Communications in Nonlinear Science and Numerical Simulation 111 (2022) 106484

Contents lists available at ScienceDirect

Communications in Nonlinear Science and Numerical Simulation

journal homepage: www.elsevier.com/locate/cnsns

Coriolis coupling in a Hénon–Heiles system

J.P. Salas [a,*], V. Lanchares [b], M. Iñarrea [a], D. Farrelly [c]

[a] *Área de Física Aplicada, Universidad de La Rioja, 26006 Logroño, Spain*
[b] *Departamento de Matemáticas y Computación, Universidad de La Rioja, 26006 Logroño, Spain*
[c] *Department of Chemistry and Biochemistry, Utah State University, Logan, UT 84322-0300, USA*

ARTICLE INFO

Article history:
Available online 1 April 2022

Keywords:
Nonlinear dynamics
Escape dynamics
Chaotic behavior

ABSTRACT

We study the impact of a Coriolis term in the dynamics of a perturbed Hénon–Heiles Hamiltonian. The strength of the Coriolis coupling is measured by a frequency ω that regulates two different regimes. If (in scaled units) ω1, the minimum becomes a dynamically stable maximum, and there appears an open region of stable motion around that maximum. We restrict our study to $\omega \in [0, 1)$ because we find richer dynamics in that interval. Poincaré surfaces of section are used to show how the strength of the Coriolis coupling controls the size of the trapping area. While, for $\omega = 0$, most of the orbits escape, for $\omega \approx 1$ most of the orbits remain trapped. The transition from one situation to the other one reveals complex resonant structures giving rise to a chaotic sticky region of long living orbits. The study of the escape basins reveals that they evolve from a complex structure, with fractal boundaries, to basins with smooth boundaries. Explicit computation of the evolution of the basin entropy confirms this fact. The escape probability as a function of ω is also calculated. Both the evolution of the escape probability and the entropy are not monotonic and exhibit intricate and complex dynamics for intermediate values of ω.

1. Introduction

The Hamiltonian dynamics of systems in which an (often) non-conserved Coriolis term is present continues to be an area of current research. Examples in atomic and molecular physics are atoms and molecules interacting with crossed electric and magnetic fields [1–7], and with circularly and elliptically polarized electromagnetic fields [8–14], including the particular case of optical centrifuge for molecules [15–18]. Another, more recent, example is the control of high-order harmonic generation (HHG) in molecules by using multi-frequency circularly polarized rotating (and counter-rotating) combinations of laser pulses [19,20]. This is currently an active area of research with applications in photonics and nanotechnology, as well as in other areas. In general, the HHG Hamiltonian contains a zero-order molecular Hamiltonian plus a non-conserved Coriolis term, and a time dependent driving interaction [20]. The dynamics can be understood qualitatively in terms of the competition between the Coriolis and driving terms. Essentially the electron escapes from the parent ion by tunneling and is then controlled by the laser field — the driving terms in the Hamiltonian. The electron may eventually undergo a re-collision with the parent ion, and depending on the symmetry of the ion, HHG may occur. Controlling the strength of the Coriolis term allows for control of the polarization and energies of the harmonics generated. Both 2D and 3D systems have been studied using Hamiltonian models (e.g., Ref. [21]). Coriolis coupling also occurs in

* Corresponding author.
E-mail address: josepablo.salas@unirioja.es (J.P. Salas).

https://doi.org/10.1016/j.cnsns.2022.106484

rovibrational spectroscopy, however, it is often weak and may often be neglected. Here, we are interested in situations where the Coriolis coupling plays a dominant role.

Other areas in which Hamiltonians with Coriolis couplings arise are astronomy and galactic dynamics. For example, in the very well-known restricted three body problem, a Coriolis term is responsible for most of the dynamics in that system. Besides this case, the book by Binney and Tremaine [22] emphasizes the necessity of considering rotating potentials to better explain the dynamics of stellar orbits in a galaxy, as well as the evolution of the disk galaxies [23]. In this setting, equilibrium points and periodic orbits play an important role, as they organize the phase flow structure and different qualitative aspects of the dynamical system can be understood. An interesting example is the possibility of matter transfer through heteroclinic connections between equilibrium points, a mechanism proposed to explain the formation of spiral arms [24]. Of more general interest is the determination of periodic orbits, mainly used to classify different types of motion that can account, for instance, for the existence of unusual rotating barred galaxies [25–27]. Although many studies of barred galaxies involve explicit N-body simulations, it is possible to construct autonomous Hamiltonian systems with a "frozen" potential which represents a snapshot of the N-body simulation [28]. This class of model allows more direct insight into the underlying dynamical processes. A recent example is a study of the so-called peanut-shaped disk galaxies [25]. The main finding is that periodic orbits, nearby quasiperiodic and sticky orbits control the structure of the galaxy. This phenomenon has also been observed in simulations of the capture of irregular moons by the giant planets and the formation of binaries in the Kuiper belt [29–31]. In each of these cases, the Coriolis term plays a significant role and it is central to know how the dynamics evolve.

A more general context where a Coriolis term appears is in open time-independent Hamiltonian systems. These systems are characterized by the existence, in phase space, of one or more escape channels. Then, we can generically find two types of trajectories: those that remain trapped in the interaction region (*interior*), and those that escape to infinity (*exterior*) through one of the escape channels. The reason why a given orbit has or does not have access to a certain escape channel is far for being a simple question. However, we know that the interior and the exterior regions are connected through a bottleneck (i.e., a *transition state*), and each transition state is associated with a specific saddle point. In this sense, very important investigations of, among others, Wiggins and coworkers [32–36] have contributed to the development of a theory, that, under certain conditions, allows one to make an analytic construction of the dividing surfaces that in phase space separate escape and non-escape trajectories. The most important requirement of that theory is that no trajectory passes through a dividing surface more than once. However, it is well known that in many cases, as for example for high enough energy trajectories, a given orbit may cross the dividing surface several times, so that the "no recrossing" requirement of the theory fails. Then, when there are recrossings, it is not possible to decide whether or not a given orbit will escape. Furthermore, when there is more than one escape channel, it is also hard to decide not only if the orbit will escape, but also the channel through which the escape will take place. In the latter situation, the study of the so-called escape basins is a very useful tool to get a global vision of the escape or scattering dynamics, and it has been used in as varied branches of science as nonlinear dynamics (see e.g. [37–40]), atomic physics [41] or astronomy and astrophysics [42].

Every escape channel of an open Hamiltonian system defines a escape basin, which is usually taken to be the set of initial conditions leading to trajectories that escape through a given channel. Because there also exits a basin for the non-escape orbits in any scattering process, and although our system is conservative, we will speak generically of attraction basins to designate both escape and non-escape basins. Furthermore, when the boundaries between the basins are smooth curves, the final destination of the orbits belonging to those basins is completely predictable. Conversely, there are scattering processes where boundaries are not well defined, such that it is impossible, or almost impossible, to predict the future an orbit. In this case, those scattering processes are chaotic and the boundaries between basins are fractal structures (see e.g. [43–45]) that, in many cases, follow the more restrictive property of Wada [37,46–48].

In most studies, energy is the only relevant parameter of the evolution of the structure of the escape basins and, in general, in the escape dynamics. However, there are many examples were, besides the energy, the Hamiltonian depends on additional parameters; one class being systems with a non-conserved Coriolis term. For these systems, we desire to understand how the escape dynamics depends on the strength (as measured by the frequency, ω) of the Coriolis coupling absent other perturbations. For this purpose, we choose as our case study the 2D Hénon–Heiles Hamiltonian, to which we add a Coriolis term. The Hénon–Heiles model was originally introduced in the context of galactic dynamics [49] but has been widely studied in chemistry and physics, for example, as a model of coupled normal modes and chaotic dynamics in general [37,50].

The article is organized as follows: Section 2 introduces the Hamiltonian and describes some basic properties of the system, including the nature and positions of the various equilibria. To accomplish this, an effective potential (or, zero-velocity surface [51]) is introduced and its structure and equilibria studied as a function of ω and the energy. A significant observation is that trapped trajectories and periodic orbits may exist for energies above the three saddle points in the Henon–Heiles potential. Section 3 proceeds to examine the escape dynamics using Poincaré surfaces of section. We find that, as $\omega \to 1$ (in scaled units), most of the orbits will be trapped, although the size of the scattering region goes to zero in this limit. For values of ω intermediate between 0 and 1 a substantial chaotic zone develops with orbits being temporarily trapped in sticky regions of phase space. Section 4 examines the evolution of the structure of the escape basins. Escape probabilities are computed from the escape basins as ω is varied, and the behavior of the escape probability is explained in terms of the basin entropy. In Section 5 the evolution of the escape probability as a function of ω is calculated taking into account all the phase space volume. The results are in excellent agreement with those obtained using the escape basins. Conclusions are presented in Section 6.

2. The Hamiltonian system and basic properties

Let us consider the rotating Hénon–Heiles system defined by the Hamiltonian function

$$\mathcal{H} = \frac{1}{2}(X^2+Y^2) + \frac{1}{2}(x^2+y^2) - \omega(xY - yX) + yx^2 - \frac{1}{3}y^3, \tag{1}$$

where (x, y) and (X, Y) are the cartesian coordinates and their corresponding canonical momenta. Finally, $\omega \in \mathbb{R}$ is the frequency of the Coriolis coupling term. The Hamiltonian equations of the motion are given by

$$\begin{aligned} \dot{x} &= \frac{\partial \mathcal{H}}{\partial X} = X + \omega y, \quad \dot{X} = -\frac{\partial \mathcal{H}}{\partial x} = -x + \omega Y - 2xy, \\ \dot{y} &= \frac{\partial \mathcal{H}}{\partial Y} = Y - \omega x, \quad \dot{Y} = -\frac{\partial \mathcal{H}}{\partial y} = -y - \omega X - x^2 + y^2. \end{aligned} \tag{2}$$

The system inherits some of the properties of the classical model, when $\omega = 0$. In this sense, it is invariant under the action of the cyclic group C_3 and also symmetric with respect to the planes

$$x = 0, Y = 0, \qquad x = \sqrt{3}y, Y = \sqrt{3}X, \qquad x = -\sqrt{3}y, Y = -\sqrt{3}X. \tag{3}$$

Thus, coordinates and momenta are invariant under the dihedral group D_3 separately. Moreover, the system enjoys the additional symmetry

$$S \equiv \mathcal{H}(x, y, X, Y; \omega) = \mathcal{H}(x, y, -X, -Y; -\omega), \tag{4}$$

implying that it is enough to consider positive or negative values of the frequency ω. The equilibrium points of the system are the roots of the Hamiltonian flux (2) equated to zero. In this way, it is straightforward to show that there are four equilibrium points (x_e, y_e, X_e, Y_e) for the system (1), namely

$$\begin{aligned} E_0 &\equiv (0, 0, 0, 0), \\ E_1 &\equiv \left(0, 1-\omega^2, \omega(\omega^2-1), 0\right), \\ E_2 &\equiv \left(\tfrac{\sqrt{3}}{2}(1-\omega^2), \tfrac{1}{2}(\omega^2-1), \tfrac{1}{2}\omega(1-\omega^2), \tfrac{\sqrt{3}}{2}\omega(1-\omega^2)\right), \\ E_3 &\equiv \left(\tfrac{\sqrt{3}}{2}(\omega^2-1), \tfrac{1}{2}(\omega^2-1), \tfrac{1}{2}\omega(1-\omega^2), \tfrac{\sqrt{3}}{2}\omega(\omega^2-1)\right). \end{aligned} \tag{5}$$

A close look at the coordinates of the equilibrium points reveals the presence of the symmetries previously mentioned. On the one hand, the coordinates of the equilibrium points in the configuration space only depend on ω^2, due to the S symmetry. Furthermore, as a consequence of the C_3 symmetry, the coordinates (x, y) and (X, Y) of the three critical points E_j, $j \neq 0$, define two equilateral triangles, whose barycenters are at the origin, being the length of their sides $\ell_{(x,y)} = \sqrt{3}|1-\omega^2|$ and $\ell_{(X,Y)} = \sqrt{3}|(1-\omega^2)\omega|$, respectively. Besides, the triangle in the (x, y) coordinates is symmetric with respect to the y axis, whereas the triangle in the (X, Y) momenta is symmetric with respect to the X axis, by virtue of the symmetry (3).

The stability analysis of the equilibrium E_0 yields that it is linearly stable, provided the four eigenvalues of the stability matrix associated to (2) appear as two pure complex conjugate pairs (see [52])

$$\lambda^0_{1,2} = \pm i(1+\omega), \quad \lambda^0_{3,4} = \pm i(1-\omega). \tag{6}$$

In addition, it is also stable in the Lyapunov sense for every value of $\omega \neq 1$ (see [53]). On the contrary, $E_{1,2,3}$ are unstable because the four eigenvalues of the corresponding stability matrix appear as a pure complex conjugate pair $\lambda_{1,2}$ and a real pair $\lambda_{3,4}$ given by

$$\lambda_{1,2} = \pm i\sqrt{1+\omega^2+2\sqrt{\omega^4-\omega^2+1}}, \quad \lambda_{3,4} = \pm\sqrt{-1-\omega^2+2\sqrt{\omega^4-\omega^2+1}}. \tag{7}$$

Indeed, $E_{1,2,3}$ are center $\times$ saddle points lying on the same energy manifold

$$\mathcal{H} = \mathcal{E}_e = \frac{(1-\omega^2)^3}{6}, \tag{8}$$

and on the three dimensional sphere

$$x^2 + y^2 + X^2 + Y^2 = (1+\omega^2)(1-\omega^2)^2 = R^2. \tag{9}$$

Moreover, the distance between any pair of critical points (E_i, E_j), $i, j \neq 0$, is constant and equal to $\sqrt{3}R$. Note that the distance tends to 0 as ω tends to 1, so that the four equilibria collide when $|\omega| = 1$, where a bifurcation takes place. After this bifurcation, we recover the four critical points with the same linear stability character. However, there is a change in the energies. For $|\omega| < 1$, $\mathcal{E}_e > 0$, which is bigger than the energy $\mathcal{E}_0 = 0$ of E_0. On the contrary, for $|\omega| > 1$, $\mathcal{E}_e < 0$ and it is below the energy $\mathcal{E}_0 = 0$. This change in the relative values of the energies of the equilibrium points can be illustrated through the zero velocity curves associated to the effective potential $U(x, y)$ defined as [51]

$$U(x, y) = \mathcal{H} - \frac{1}{2}(\dot{x}^2+\dot{y}^2) = \frac{1-\omega^2}{2}(x^2+y^2) + x^2y - \frac{1}{3}y^3. \tag{10}$$

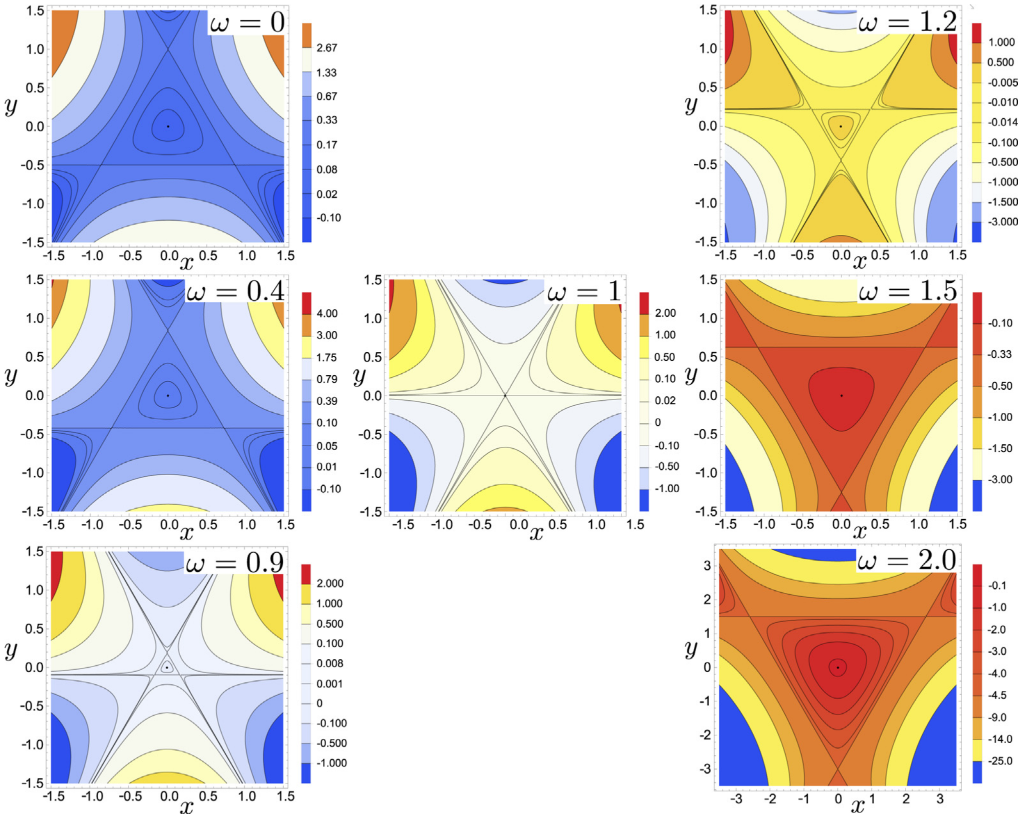

Fig. 1. Contour levels of the effective potential $U(x, y)$ (see Eq. (10)) for different values of ω.

Because the critical points of $U(x, y)$ match the coordinates of the equilibrium points $E_{0,1,2,3}$, the evolution of the landscape of $U(x, y)$, for varying $|\omega|$, will give us information about the transition through the bifurcation. When $|\omega| < 1$, the contour levels of $U(x, y)$ for $\omega < 1$, depicted in the left panels of Fig. 1, show that E_0 is a minimum, and that there is a trapping region inside the triangle whose vertices are $E_{1,2,3}$. For $|\omega| > 1$, E_0 becomes a maximum (see the contour plots of $U(x, y)$ in the right panels of Fig. 1 for $\omega > 1$). At this point, we recall that, despite its character, the equilibrium E_0 is always stable [53]. There is also a change in the disposition of the critical points. For $|\omega| < 1$, E_1 is located at the positive y axis and $E_{2,3}$ at the semiplane $y < 0$. On the contrary, for $|\omega| > 1$, E_1 is on the negative y axis and $E_{2,3}$ in the semiplane $y > 0$. Besides, as $|\omega| \to \infty$ the saddle points tend also to infinity and the contours levels resemble those of the function

$$U_\infty = \frac{1-\omega^2}{2}(x^2 + y^2),$$

which corresponds to the effective potential of two isotropic harmonic oscillators coupled by the Coriolis term. In this way, one expects that the system will behave in a regular manner as $|\omega|$ increases far away $|\omega| = 1$, at least in a wide part of the phase space.

From the discussion above, there are two different regimes, depending on the value of the frequency ω. For $|\omega| < 1$, trapped motion exists for values of the energy below $\mathcal{E}_e$, whereas as soon as the energy is greater than $\mathcal{E}_e$, trajectories can escape to infinity through three channels in the vicinity of the saddle points. However, the trap region shrinks with increasing $|\omega|$ and disappears as soon as the bifurcation takes place at $|\omega| = 1$. For $|\omega| > 1$ there is not a trapping region in the usual sense, because E_0 is a maximum. However, the stable nature of this maximum E_0, for $|\omega| > 1$, makes possible the existence of confined orbits in a neighborhood E_0. Two examples of trapped trajectories for $\omega = 2$ and energies $\mathcal{E} = \pm 1$ are shown in Fig. 2. In this work we will focus in the dynamics for the case $|\omega| < 1$ and, more precisely, in how the frequency ω affects the escape dynamics.

3. Escape dynamics for $\omega < 1$

In this section, to study the escape dynamics of the system, we fix the energy $\mathcal{E}$ while we vary the frequency ω. Due to the symmetry S (see Eq. (4)), we reduce to values of ω in the interval $[0, 1)$. As the energy $\mathcal{E}_e$ of the unstable equilibria

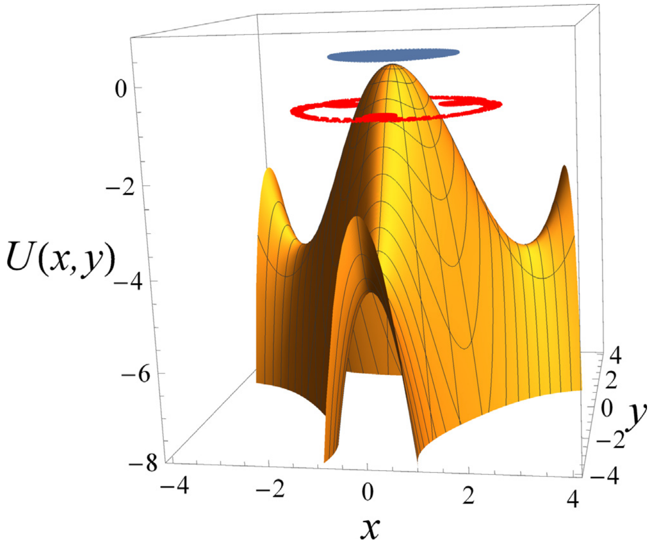

Fig. 2. Examples of two trapped trajectories for $\omega = 2$ and energies $\mathcal{E} = 1$ (blue orbit) and $\mathcal{E} = -1$ (red orbit).

depends on ω, in order to make the results comparable to each other, we will fix the value of system energy $\mathcal{E}$ to be 20% higher than $\mathcal{E}_e$. That is to say, we choose an energy

$$\mathcal{E} = \frac{(1-\omega^2)^3}{5}. \tag{11}$$

We are interested in the effect the frequency ω produces in the escape dynamics. This can be viewed through Poincaré surfaces of section. To this end, a convenient Poincaré map is $x = 0$ when it is crossed in the direction $\dot{x} > 0$. After introducing these conditions in the Hamiltonian (1), the Poincaré sections appear in the (y, Y) plane, and they are limited by the curve

$$Y^2 + (1-\omega^2)y^2 - \frac{2}{3}y^3 = 2\mathcal{E}. \tag{12}$$

For $\mathcal{E} > \mathcal{E}_e$, Eq. (12), is an open curve, and it is clear that the size of the inner region of the section tends to zero as $\omega \to 1$, in accordance to the evolution of the distance between the unstable critical points. Furthermore, we expect that, as $\omega \to 1$, most of the orbits are trapped due to two facts. On the one hand, the available phase space region around the minimum and the bottlenecks around the saddle points (i.e., the scattering region) tends to zero as $\omega \to 1$. On the other hand, the Lyapunov stability implies that there exists a sufficient small neighborhood of the origin were the orbits remain trapped. So, one expects that the intersection of both regions contains the majority of the orbits.

In Fig. 3 we show a gallery of surfaces of sections for values of ω ranging from 0 to 0.9. To better visualize the escape dynamics, in Fig. 3, the intersection of the orbits with the Poincaré plane has been computed in the time interval $t \in [500, 1500]$. In this way, only the trajectories with an escape time belonging to that interval are considered as orbits with a long enough *trapping time* to contribute, before eventually escape, to the phase space structure.

It can be seen in Fig. 3(a) that, for $\omega = 0$, almost all the trajectories escape, except for those appearing in two tiny regions around two stable fixed points located at the $Y = 0$ axis, that correspond to the same stable periodic orbit. The blue circles guide the eye to locate these tiny regions of confined motion. Moreover, Fig. 4(a) depicts the clover-like periodic orbit around which the confined motion is organized. When $\omega = 0.1$, the region of non-escape orbits becomes larger. However, the region diminishes up to $\omega \approx 0.2$ (see Fig. 3(a)–(b)) to grow again monotonically in such a way that, for values of ω close to 1, most of the surface of section is dominated by robust KAM tori around a stable periodic orbit (see Fig. 3(g)–(h)). More specifically, this stable periodic trajectory is an almost circular orbit and it is depicted, together with two quasi periodic trajectories around it, in Fig. 4(b) for $\omega = 0.9$. From the evolution of the Poincaré maps shown in Fig. 3, the global effect of the frequency ω on the system dynamics is twofold. On the one side, as ω increases, the number of escape orbits strongly decreases, so that for values of ω close to 1, most of the orbits in the scattering region around the potential well are trapped and exhibit regular behavior. On the other side, the available scattering region around E_0 decreases for increasing frequency.

In the transition from mainly escape to mainly trapped orbits, there is an interesting situation in the interval $0.3 \lesssim \omega \lesssim 0.5$ that can be observed in Figs. 3(e)–(f), in which the periodic orbit I_C plays a relevant role. When decreasing ω between $\omega \approx 0.5$ and $\omega \approx 0.3$, it can be seen that the KAM tori around I_C are replaced by a wide stochastic layer. The reason of this change is a bifurcation of the periodic orbit I_C. Indeed, the computation of the stability index κ (see Fig. 5),

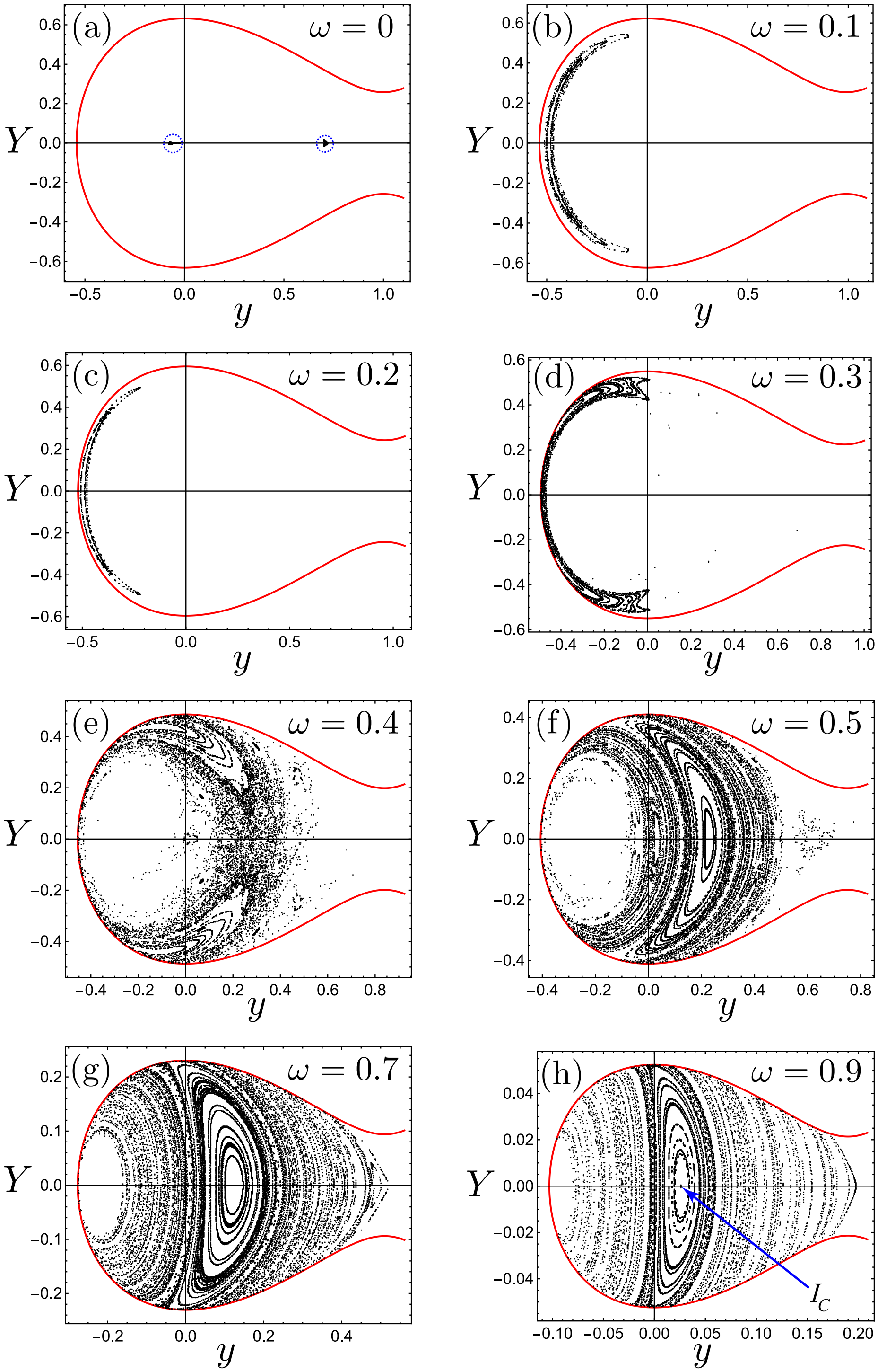

Fig. 3. Poincaré surfaces of section, $x = 0$, $\dot{x} > 0$, for $\mathcal{E} = 1.2\mathcal{E}_e$ and $0 \le \omega \le 0.9$. The blue circles in panel (a) guide the eye to locate the tiny regions of confined motion. The fixed point I_C in panel (h) is a stable almost circular periodic trajectory that is depicted in Fig. 4(a). The red lines are the limit of the Poincaré sections.

defined as the trace of the monodromy matrix [54], reveals that the orbit I_c undergoes a period doubling bifurcation at $\omega \approx 0.48$. From this bifurcation, I_c becomes unstable and, at the same time, two new stable periodic orbits born. As a consequence, it can be observed in Fig. 3(e) that different resonant structures, surrounded by zones of chaotic motion,

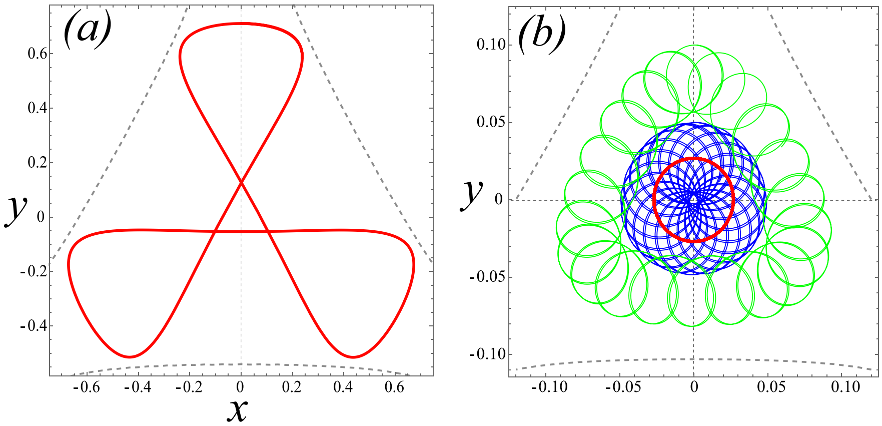

Fig. 4. (a) The red orbit is the stable periodic trajectory located inside the blue circles in the Poincaré section Fig. 3(a) for $\omega = 0$. The coordinates of this orbit on the section of Fig. 3(a) are ($y \approx 0.7115$, $Y = 0$). (b) The red curve is the stable almost circular periodic trajectory that corresponds to the fixed point labeled as I_C in the Poincaré section Fig. 3(h). The blue and green orbits are quasiperiodic trajectory around I_C. The coordinates of those orbits on the section of Fig. 3(h) are ($y \approx 0.0268$, $Y = 0$), ($y = 0.05$, $Y = 0$) and ($y = 0.1$, $Y = 0$), respectively. The black dashed lines in both figures correspond to the equipotential curves $U(x, y) = \mathcal{E} = 1.2\ \mathcal{E}_e$.

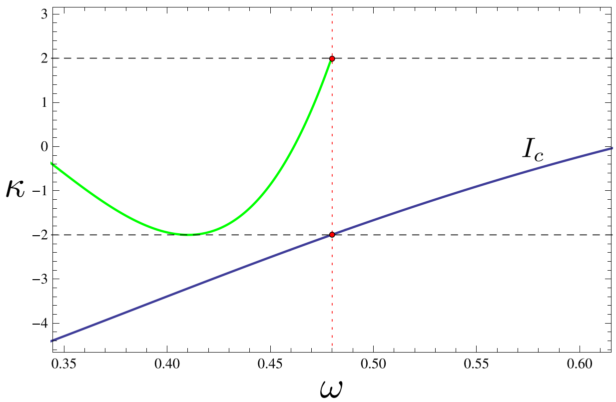

Fig. 5. Evolution of the stability index κ of the orbit I_C (blue line) as function of ω. At $\omega \approx 0.48$ the stability index of I_C reaches the critical value $\kappa = -2$, and a period doubling bifurcation takes place. A new family of stable periodic orbits appear (green line).

appear. The existence of these chaotic regions correspond to long living sticky orbits. To better visualize this situation, a zoom of the surface of section in Fig. 3(e) is computed considering the intersections with the Poincaré plane during 1000 units of time after different increasing threshold times. Fig. 6 shows four surfaces of section for $\omega = 0.4$ computed in different time intervals (a) $t \in [500, 1500]$, (b) $t \in [5000, 6000]$, (c) $t \in [10000, 11000]$ and (d) $t \in [15000, 16000]$. In Fig. 6(a) we can clearly see the region of sticky orbits. However, as the limits of the time intervals increase, there is a progressive disappearance of the chaotic sticky orbits (see 6(b)–(d)). We can also observe in Fig. 6 the presence of robust complex resonant structures around stable periodic orbits that appear giving rise to the aforementioned sticky region of long living orbits in the scattering region. This is an interesting phenomenon that has been proposed to explain the shape of some barred galaxies [25–27]. Finally, Fig. 7 shows a gallery of some of those stable periodic orbits living into the resonant structures. It is worth noting the presence of periodic orbits enjoying the C_3 symmetry (upper panels of Fig. 7), each of them representing a single periodic orbit. However, periodic orbits in the lower panels of Fig. 7 give rise to two more periodic orbits, by applying the C_3 symmetry.

4. Evolution of the escape basins. Escape probability

4.1. Evolution of the escape basins

For energy values $\mathcal{E}$ above the saddle point energy $\mathcal{E}_e$, the rotating Hénon–Heiles is an open Hamiltonian system with three equiprobable escape channels. Furthermore, the evolution of the Poincaré sections of Fig. 3 shows that, for increasing values of ω, most of the escape orbits appearing for small values of ω are gradually replaced by regular confined orbits.

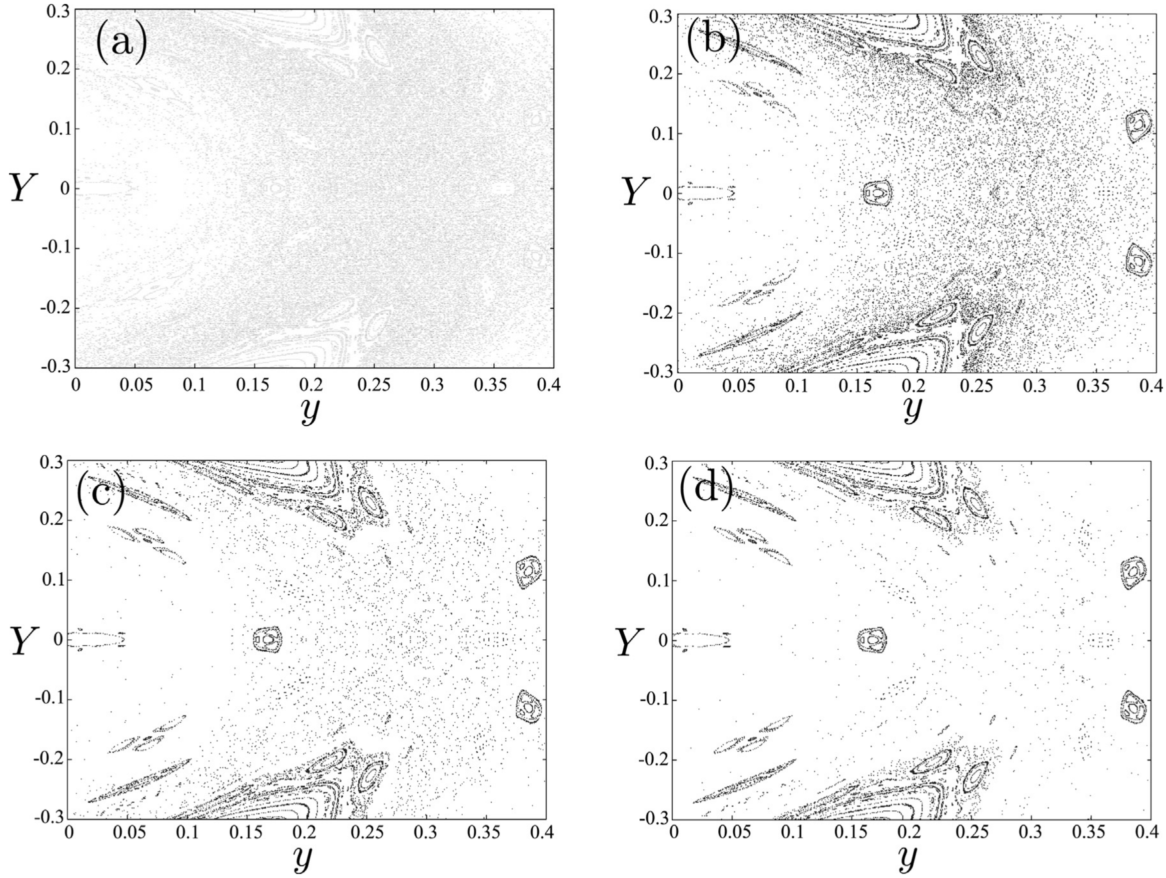

Fig. 6. Poincaré surfaces of section, $x = 0$, $\dot{x} > 0$, for $\mathcal{E} = 1.2\mathcal{E}_e$, $\omega = 0.4$ and different intervals of time. (a) $t \in [500, 1500]$, (b) $t \in [5000, 6000]$, (c) $t \in [10000, 11000]$ and (d) $t \in [15000, 16000]$.

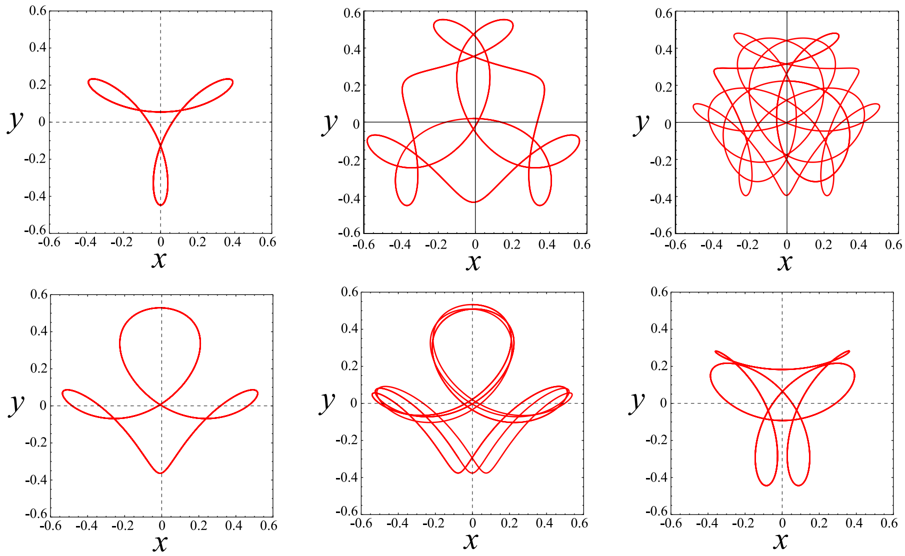

Fig. 7. Gallery of stable periodic orbits living into some of the resonant structures that appear in Fig. 6.

Thus, for $\mathcal{E} > \mathcal{E}_e$ and for a given value of ω, there are four possible final outcomes or *attractors* for any trajectory, three of them correspond to an escape trajectory through the saddle points, while the remaining one corresponds to a trapped orbit. Thus, we expect to find in phase space four basins of attraction, each of them determining the future of a given set of initial conditions. Furthermore, the boundaries between the different basins provide very useful information because their topology is closely related to the dynamics displayed by the system [37,44,45]. Then, it is natural to study how the Coriolis coupling affects the structure of those attraction basins for increasing values of ω.

The determination of the attraction basins of our system starts by defining a fine grid of initial conditions covering the available phase space. Then, every of those initial conditions is propagated by solving the Hamiltonian equations of motion (2). The resulting trajectories are followed until they escape through one of three channels or remain trapped up to a very long cut-off time t_f. If a trajectory leaves the scattering region through the saddle point E_1, we label that trajectory as belonging to basin 1. The same applies for the saddle points $E_{2,3}$. On the other hand, if for $t \geq t_f$ a trajectory remains wandering in the scattering region, we assume that the trajectory belongs to the trapping basin and it is labeled with 0. Because the rotating Hénon–Heiles system is a time-independent two-degrees of freedom Hamiltonian system in the phase variables (x, y, X, Y), trajectories evolve in a three-dimensional space described by three of these variables, being the remaining one fixed by the constrain $\mathcal{H} = \mathcal{E}$. Then, in this problem, the grid of initial conditions is actually a three-dimensional partition and, therefore, the attraction basins are also three dimensional objects. Besides the computational cost of the numerical propagation of a huge number of initial conditions that entails a three-dimensional grid, we encounter the additional problem of a useful visualization of the basins. Thence, we find more convenient to handle a planar representation of the basins, which involves choosing a planar set of initial conditions as well. More specifically, we select the initial conditions following the procedure proposed in [37]. In terms of the velocities $(\dot{x}, \dot{y})$, and using the zero velocity surface $U(x, y)$ (see Eq. (10)), the Hamiltonian (1) reads as

$$\mathcal{H} = \mathcal{E} = \frac{1}{2}(\dot{x}^2 + \dot{y}^2) + U(x, y), \tag{13}$$

where $(\dot{x}, \dot{y}) = (X + \omega\, y, Y - \omega\, x)$. Then, for fixed values of ω and $\mathcal{E}$, the available set of initial conditions in the configurations space is given by $\mathcal{D}_{x,y} = \{(x, y)|\ U(x, y) \leq \mathcal{E}\}$. For each vector $\mathbf{r} = (x, y) \in \mathcal{D}_{x,y}$, the velocity vector $\mathbf{v} = (\dot{x}, \dot{y})$ is chosen as $\mathbf{r} \cdot \mathbf{v} = 0$ with the vector $\mathbf{r} \times \mathbf{v}$ pointing in the positive sense. In all our computations we have checked that, with this choice of the initial conditions, the three escape channels are equiprobable with a 95% confidence level, which indicates that this choice provides us a suitable glimpse of the escape basins. Therefore, the basins can be depicted in the planar domain $\mathcal{D}_{x,y}$. In Fig. 8, for energy values 20% higher than $\mathcal{E}_e$ and for increasing values of ω, a gallery of escape basins is shown. The color code in Fig. 8 assigns the red, green and blue colors to initial conditions escaping through exits E_1, E_2 and E_3, respectively. The black color is assigned to the initial conditions of orbits that, after the cut-off time $t_f = 2 \times 10^4$ remain trapped in the scattering region, such that these trajectories are labeled as non-escape events. In this way, regions with the same color shape each of the four possible attraction basins in the domain $\mathcal{D}_{x,y}$.

For the non-rotating case $\omega = 0$, the escape basins depicted in Fig. 8(a) indicates that most of the trajectories escape. Indeed, we observe disjoint basins where the exit of the trajectories is clear. However, those disjoint regions are mostly separated from each other by wide boundaries where it is almost impossible to predict the final state of a given orbit. This fact was extensively studied by Aguirre et al. [37], showing that the escape basins for $\omega = 0$ have fractal structure satisfying the Wada property [46–48], which confirms the high unpredictability observed in Fig. 8(a).

For $\omega > 0$, Fig. 8 shows that significant black regions corresponding to non-escape basins appear. Interestingly, the evolution of these black basins is non-monotonic. Namely, for $\omega = 0.1$ and 0.15, the size of the black basins seems to increase; for ω between 0.2 and 0.4 its size decreases while, for $\omega > 0.4$, the black basins grow in size, such that for $\omega = 0.8$, a unique non-escape basin occupies a large region of the domain $\mathcal{D}_{x,y}$. This non-monotonic evolution of the basins shows the complexity of the dynamics for intermediate values of ω. On the other side, the large size of the black basin for $\omega \gtrsim 0.6$ reveals the stabilizing role of ω. This result is in agreement with the one provided by the Poincaré sections where, for high enough ω, a large phase space region is occupied by non-escape orbits living in the neighborhood of a stable periodic orbit.

Besides its influence in the stabilizing and confining of the orbits, the evolution for increasing ω of the structure of the boundaries between the basins is also an important aspect. Indeed, after a general view of Fig. 8, we infer that, for intermediate values of the frequency ω (see the panels in Fig. 8 for $\omega \leq 0.5$), the boundaries between the basins are still regions with a high uncertainty. We also observe that this global uncertainty or unpredictability is significantly reduced for larger values of ω, so that, in panels Fig. 8(k)–(l) for $\omega = 0.7$ and 0.8, the boundaries between the different basins are clearly defined, in such a way that unpredictability has disappeared. Again, the evolution of the boundaries between the escape basins confirms the results we found in the study using the Poincaré sections. Namely the decrease of the chaoticity of the system (e.g., its unpredictability) for large values of ω.

In the previous discussion about the evolution of the escape basins as a function of ω, we handled unpredictability and uncertainty as fundamental concepts to understand the escape dynamics in the rotating Hénon–Heiles problem. However, from the color maps of Fig. 8, it is not possible to obtain a quantitative measure of the degree of unpredictability or uncertainty of the system for a given value of ω. In order to measure the intrinsic unpredictability in scattering processes, Daza et al. [45] proposed a correlation function named *basin entropy*, which is based on the Gibss entropy expression. In a nutshell, given a dynamical system with N_A attractors, let suppose we discretize the phase space in N_B small boxes B_i, $\forall i = 1, \ldots, N_B$. Inside each of those boxes, we considered a high enough number N of initial conditions. Each of the N

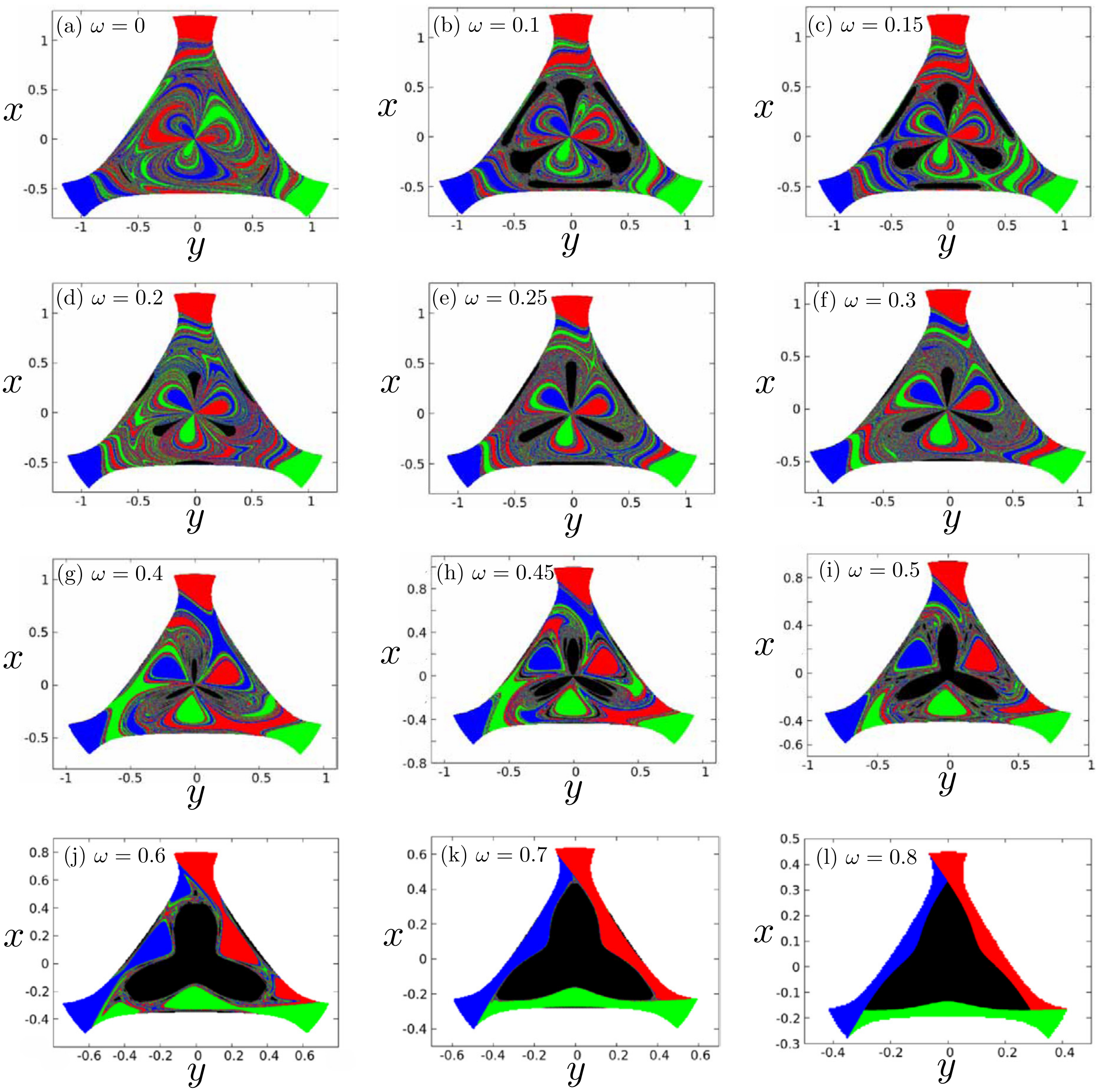

Fig. 8. Evolution of the escape basins of the rotating Hénon–Heiles system for increasing values of the frequency ω.

initial conditions inside the box B_i is propagated, such that its corresponding final basin is determined. Then, if p_{ij} is the probability that the basin j occurs in the box B_i, the Gibbs entropy S of the basins is given by

$$S = \sum_{i=1}^{N_B} \sum_{j=1}^{N_A} p_{ij} \ln \left(\frac{1}{p_{ij}} \right). \tag{14}$$

The function S provides useful information about the degree of uncertainty of the system because, when $S = 0$, there is only one attraction basin, while if the system is completely chaotic with N_A equiprobable attractors, we have the maximal entropy value $S_{max} = N_B \ln N_A$. In order to avoid in (14) the dependence on N_A and N_B, we define the normalized entropy $\widehat{S} = S/S_{max}$, such that $0 \le \widehat{S} \le 1$. In this way, by using Eq. (14), we compute, for different values of ω, the basin entropy $\widehat{S}$ of the corresponding escape basins. In our case, the boxes B_i, $\forall i = 1, \dots, N_B$, are squares of linear size ϵ that define a planar grid that spans the domain $\mathcal{D}_{x,y}$. In [45], it is shown that, even though that $\widehat{S}$ depends on the chosen value of ϵ, while the scaling box size ϵ is fixed, the value of $\widehat{S}$ converges for increasing number of trajectories inside a box. In our case, we propagate thirty six trajectories in each squared box. The results of these calculations are shown in Fig. 9 for two scaling box sizes $\epsilon = 10^{-3}$ and $\epsilon = 2 \times 10^{-3}$. As expected, the evolution of the basin entropy $\widehat{S}$ is qualitatively the same

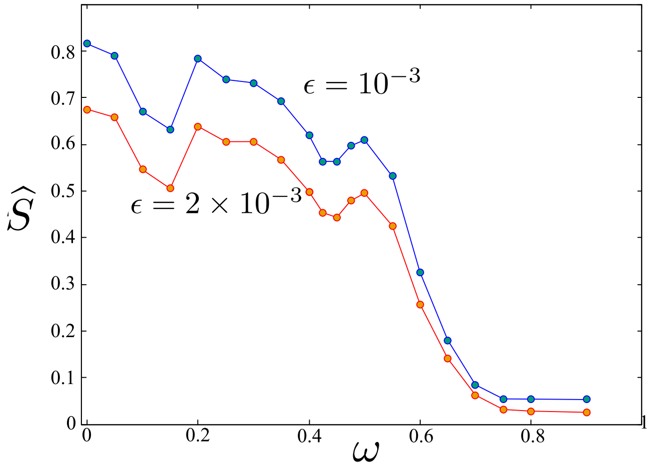

Fig. 9. Evolution of the normalized basin entropy $\widehat{S}$ of the rotating Hénon–Heiles system for increasing values of the frequency ω. Two scaling box sizes $\epsilon = 10^{-3}$ and $\epsilon = 2 \times 10^{-3}$ have been used in the calculation.

for both values of ϵ. On the other hand, $\widehat{S}$ shows a global decreasing for increasing ω, such that, for large values of ω, the basin entropy tends asymptotically to zero. This indicates (see Fig. 8 for $\omega = 0.8$) that the unpredictability in the escape dynamics almost disappears, so that the system becomes deterministic. However, the behavior of $\widehat{S}$ is non-monotonic, showing two minima around $\omega \approx 0.15$ and $\omega \approx 0.45$ respectively. Interestingly, the increasing of the size of the non-escape black basins observed in Fig. 8, for ω between 0.1 and 0.2, is a possible explanation for the local decreasing of the basin entropy around $\omega \approx 0.15$.

4.2. Escape probability

From the computation of the escape basins of the previous section, we can also obtain the escape probability associated to those basins. Then, and following the same procedure used for the calculation of the attraction basins of Fig. 8, in Fig. 10 is presented the escape probability $P(\omega)$ for ω ranging from 0 to 0.95 at steps of 0.025. Although, at a first glance, we find in Fig. 10 the expected global decreasing of $P(\omega)$, its behavior is far from being smooth. Since we start with $\omega = 0$, the escape probability is roughly one in agreement with the Poincaré section of Fig. 3(a) and with the escape basin of Fig. 8(a). In the interval $0 < \omega \lesssim 0.4$, we observe that $P(\omega)$ shows a fluctuating behavior that confirms the complex evolution observed in the Poincaré surfaces of section of Fig. 3 and in the escape basins of Fig. 8 in that interval. Then, for $\omega \gtrsim 0.4$ the escape probability shows a sharply decrease. That sharply decrease for $\omega \gtrsim 0.4$ is somehow counter-intuitive because, for ω values close to 1, one would expect that $P(\omega)$ tends to a given constant value, and this is not the behavior depicted in Fig. 10. One possible reason why $P(\omega)$ shows that monotonic decreasing even for ω values close to one is that, although the sets of initial conditions used for the computations of the escape basins preserve the equiprobable condition of the three escape channels, those sets of initial conditions do not cover all the phase volume. Therefore, the evolution of the escape probability depicted in Fig. 10 may be influenced by the way of those initial conditions were chosen. In order to test this guess, in the next section we will carry out the calculation of $P(\omega)$ using sets of initial conditions evenly distributed over all the phase space volume.

5. Escape probability

In this section we compute the escape probability by propagating samples of trajectories whose initial conditions are uniformly distributed in all the phase space volume. To this end, we choose the initial conditions $(x_0, y_0) = (x(0), y(0))$ of the orbits to be in the set

$$\begin{aligned} A(x_0, y_0) = \{&(x_0, y_0) \in \mathbb{R}^2 \mid U(x_0, y_0) \leq \mathcal{E}, \\ &y_0 \leq 1 - \omega^2, y_0 \pm \sqrt{3}\, x_0 + 2(1 - \omega^2) > 0\}, \end{aligned} \tag{15}$$

corresponding to the contour level of the zero velocity surface for a given energy $\mathcal{E}$, closed by three lines perpendicular to the three axes of the D_3 symmetry at the saddles $E_{1,2,3}$. Now, for each point belonging to $A(x_0, y_0)$, all the possible values of the initial velocity vector $(\dot{x}_0, \dot{y}_0) = (\dot{x}(0), \dot{y}(0))$ belongs to the circle

$$\dot{x}_0^2 + \dot{y}_0^2 = R(x_0, y_0; \mathcal{E})^2,$$

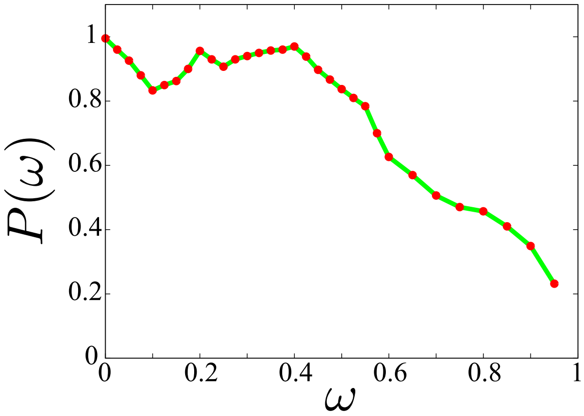

Fig. 10. Evolution of the escape probability as a function of the frequency ω. The probability has been obtained from the escape basins of Fig. 8.

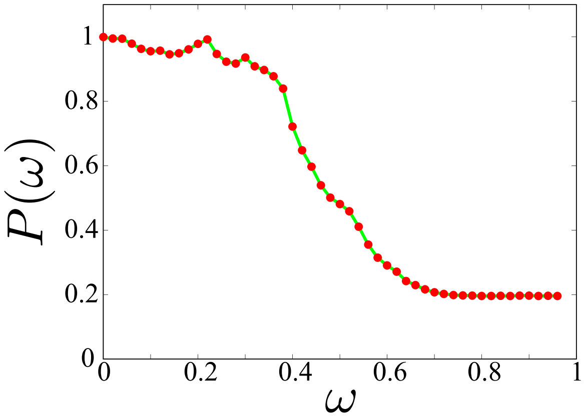

Fig. 11. Evolution of the escape probability as a function of the frequency ω in the interval $\omega \in [0, 1]$.

where $R(x_0, y_0; \mathcal{E}) = \sqrt{2(\mathcal{E} - U(x_0, y_0))}$ is the radius of that circle (see Eq. (13)). In this way, for all $(x_0 y_0) \in A(x_0, y_0)$, the possible initial momentum vectors $(X_0, Y_0) = (X(0), Y(0))$ are given by the set of points

$$\begin{aligned} B(X_0, Y_0) = \{&X_0 = R(x_0, y_0; \mathcal{E}) \cos\theta - \omega\, y_0, \\ &Y_0 = R(x_0, y_0; \mathcal{E}) \sin\theta + \omega\, x_0 \mid \theta \in [0, 2\pi)\}. \end{aligned} \tag{16}$$

Thus, the phase volume can be approximated by $A(x_0, y_0) \times B(X_0, Y_0)$ for each $(x_0, y_0) \in A$. Let be N the size of the chosen sample, (x_0, y_0, X_0, Y_0) a point of the sample and $\phi(t; x_0, y_0, X_0, Y_0)$ the orbit such that

$$\phi(0; x_0, y_0, X_0, Y_0) = (x_0, y_0).$$

If there exists $t < 2 \times 10^4$ such that $\|\phi(t; x_0, y_0, X_0, Y_0)\| > 2$, we say that the orbit escapes. Otherwise, the orbit is labeled as trapped. Now, the escape probability is defined as

$$P(\omega) = \frac{N_e}{N}, \tag{17}$$

being N_e the number of escape orbits. Fig. 11 shows the escape probability for ω ranging from 0 to 0.96 at steps of 0.02. We see the same pattern observed in the Poincaré surfaces of section. When ω is turned on, the escape probability begins to decrease. However, after $\omega = 0.1$, the probability increases until $\omega \approx 0.2$, then diminishes again, but again increases around $\omega \approx 0.35$. After that, it decreases to reach almost a constant value. If we compare the evolution of $P(\omega)$ represented in Fig. 11 with the evolution of $P(\omega)$ in Fig. 10, we observe that, for $\omega \lesssim 0.4$, in both cases the escape probability behaves qualitatively in the same way. However, there is important difference in the behavior of $P(\omega)$ for $\omega \gtrsim 0.4$. Indeed, in Fig. 11, we observe that $P(\omega)$ for $\omega \gtrsim 0.8$ shows the predicted asymptotic behavior for large ω values. Thence, as we argued in the discussion of Fig. 10, in order to compute in a correct way the escape probability of our system it is necessary to use samples of orbits with initial conditions extended to all the phase space volume.

6. Conclusions

In this paper we have studied the influence of the strength of the Coriolis coupling in the dynamics of a Hamiltonian system with a Hénon–Heiles potential. The strength of the coupling, measured in terms of the absolute value of the rotational frequency ω, regulates two different regimes. If $\omega < 1$, escape is possible through three equiprobable channels, owing to the existence of a trapping region around the minimum of the effective potential. This region shrinks as the frequency approaches unity. For $\omega > 1$, there is not a trapping region in the usual sense, because the minimum of the effective potential turns into a stable maximum. As the value of the frequency increases such that $\omega \gg 1$, the equipotential levels resemble those of a harmonic oscillator coupled by the Coriolis term and the dynamics is expected to be similar. Due to this fact, we limited our study to $\omega \in [0, 1)$ because the most rich dynamics occurs in that range. By means of Poincaré surfaces of section, it is shown how the strength of the Coriolis coupling controls the size of the trapping area in the scattering region. For $\omega = 0$, most of the orbits escape, whereas for $\omega \approx 1$ the situation is the opposite. However, the transition from one situation to the other one is not monotonic, which is revealed not only by the Poincaré sections but, also, by computing the escape probability. Even more, for intermediate values, complex resonant structures appear giving rise to a chaotic sticky region of long living orbits in the scattering region. Besides to control the escape dynamics, the strength of the Coriolis coupling has another interesting consequence. Indeed, the basins evolve from a complex structure, where the boundaries between them have fractal character, to basins with very well defined boundaries. The computation of the evolution of the basin entropy, similar to the Gibbs entropy, as a function of ω, confirms this fact. In this way, the basin entropy of the system tends to zero as the frequency approaches one, which it is consistent with the observed evolution of the Poincaré sections. Furthermore, the behavior of the entropy also confirms the decrease of the escape probability for ω approaching one. Both the evolution of the escape probability and the entropy is not monotonous, revealing the rich and complex dynamics for intermediate values of ω. In summary, the Coriolis coupling allows the formation of long living complex chaotic structures that, for high enough values of ω, become more regular compact structures.

CRediT authorship contribution statement

J.P. Salas: Conceptualization, Methodology, Validation, Software, Formal analysis, Writing – original draft, Writing – review & editing. **V. Lanchares:** Conceptualization, Methodology, Validation, Software, Formal analysis, Writing – original draft, Writing – review & editing. **M. Iñarrea:** Conceptualization, Methodology, Validation, Software, Formal analysis, Writing – original draft, Writing – review & editing. **D. Farrelly:** Methodology, Validation, Formal analysis, Writing – review & editing.

Declaration of competing interest

The authors declare that they have no known competing financial interests or personal relationships that could have appeared to influence the work reported in this paper.

Acknowledgments

This work has been partly supported from the Spanish Ministry of Science and Innovation through the Project MTM2017-88137-CO (Subprojects MTM2017-88137-C2-1-P and MTM2017-88137-C2-2-P), and by University of La Rioja through Projects REGI 2018751 and REGI 2020/15.

References

[1] Peters AD, Delos JB. Photodetachment cross section of H^- in crossed electric and magnetic fields. I. Closed-orbit theory. Phys Rev A 1993;47:3020.
[2] Peters AD, Delos JB. Photodetachment cross section of H^- in crossed electric and magnetic fields. II. Quantum formulas and their reduction to the results of the closed-orbit theory. Phys Rev A 1993;47:3036.
[3] Gourlay MJ, Uzer T, Farrelly D. Asymmetric-top description of rydberg electron dynamics in crossed fields. Phys Rev A 1993;47:3113.
[4] Neumann C, Ubert R, Freund S, Flöthmann E, Sheehy B, Welge KH, et al. Symmetry breaking in crossed magnetic and electric fields. Phys Rev Lett 1997;78:4705.
[5] Uzer T, Farrelly D. Threshold ionization dynamics of the hydrogen atom in crossed electric and magnetic fields. Phys Rev A 1995;52:R2501.
[6] Rao J, Delande D, Taylor KT. Quantum manifestations of closed orbit in the photoexcitation scaled spectrum of the hydrogen atom in crossed fields. J Phys B: At Mol Opt Phys 2001;34:L391.
[7] Rao J, Taylor KT. The closed orbits and the photo-excitation scaled spectrum of the hydrogen atom in crossed fields. J Phys B: At Mol Opt Phys 2002;35:2627.
[8] Farrelly D, Uzer T. Ionization mechanism of rydberg atoms in a circularly polarized microwave field. Phys Rev Lett 1995;74:1720.
[9] Sacha K, Zakrzewski J. H atom in elliptically polarized microwaves: Semiclassical versus quantum resonant dynamics. Phys Rev A 1998;58:3974.
[10] Mauger F, Chandre C, Uzer T. Recollisions and correlated double ionization with circularly polarized light. Phys Rev Lett 2010;105:083002.
[11] Xu Wang, Eberly JH. Classical theory of high-field atomic ionization using elliptical polarization. Phys Rev A 2012;86:013421.
[12] Kamor A, Mauger F, Chandre C, Uzer T. How key periodic orbits drive recollisions in a circularly polarized laser field. Phys Rev Lett 2013;110:253002.
[13] Yuan K-J, Bandrauk AD. Symmetry in circularly polarized molecular high-order harmonic generation with intense bicircular laser pulses. Phys Rev A 2018;97:023408.

[14] Dubois J, Chandre C, Uzer T. Nonadiabatic effects in the double ionization of atoms driven by a circularly polarized laser pulse. Phys Rev E 2020;102:032218.
[15] Karczmarek J, Wright J, Corkum P, Ivanov M. Optical centrifuge for molecules. Phys Rev Lett 1999;82:3420.
[16] Villeneuve DM, Aseyev SA, Dietrich P, Spanner M, Ivanov MYu, Corkum PB. Forced molecular rotation in an optical centrifuge. Phys Rev Lett 2000;85:542.
[17] Spanner M, Davitt KM, Ivanov MYu. Stability of angular confinement and rotational acceleration of a diatomic molecule in an optical centrifuge. J Chem Phys 2001;115:8403.
[18] Hasbani R, Ostojic B, Bunker PR, Ivanov MYu. Selective dissociation of the stronger bond in HCN using an optical centrifuge. J Chem Phys 2002;116:10636.
[19] Mauger F, Bandrauk A, Kamor A, Uzer T, Chandre C. Quantum–classical correspondence in circularly polarized high harmonic generation. J Phys B: At Mol Opt Phys 2014;47:041001.
[20] Yuan K-J, Bandrak AD. Controlling circularly polarized high-order harmonic generation in molecules by intense tricircular laser pulses. Phys Rev A 2019;100:033420.
[21] Zuo T, Bandrauk AD. Controlling harmonic generation in molecules with intense laser and static magnetic fields: Orientation effects. J Nonlin Opt Phys Mater 1995;4:533.
[22] Binney J, Tremaine S. Galactic dynamics. New Jersey, Princeton: Princeton University Press; 1994.
[23] Sellwood JA. Secular evolution in disk galaxies. Rev Modern Phys 2014;86:1.
[24] Romero-Gómez M, Masdemont JJ, García-Gómes C, Athanassoula E. The role of the unstable equilibrium points in the transfer of matter in galactic potentials. Commun Nonlinear Sci 2009;14:4123.
[25] Patsis PA, Harsoula M. Building CX peanut-shaped disk galaxy profiles. The relative importance of the 3D families of periodic orbits bifurcating at the vertical 1: 2 resonance. Astron Astrophys 2018;612:A114.
[26] Katsanikas M, Patsis PA, Pinotsis AD. Chains of rotational tori and filamentary structures close to high multiplicity periodic orbits in a 3D galactic potential. Int J Bifurcation Chaos 2011;21:2331.
[27] Katsanikas M, Patsis PA, Contopoulos G. Instabilities and stickiness in a 3D rotating galactic potential. Int J Bifurcation Chaos 2013;23:1330005.
[28] Manos T, Machado REG. Chaos and dynamical trends in barred galaxies: bridging the gap between N-body simulations and time-dependent analytical models. Mon Not Roy Ast Soc 2014;3:1.
[29] Jaffé C, Ross SD, Lo MW, Marsden J, Farrelly D, Uzer T. Statistical theory of asteroid escape rates. Phys Rev Lett 2002;89. 011101(4).
[30] Astakhov SA, Burbanks AD, Wiggins S, Farrelly D. Chaos-assisted capture of irregular moon. Nature 2003;423:264.
[31] Astakhov SA, Lee EA, Farrelly D. Formation of kuiper-belt binaries through multiple chaotic scattering encounters with low-mass intruders. Mon Not Roy Ast Soc 2005;360:401.
[32] Uzer T, Jaffé C, Palacián J, Yanguas P, Wiggins S. The geometry of reaction dynamics. Nonlinearity 2002;15:957.
[33] Jaffé C, Kawai S, Palacián J, Yanguas P, Uzer T. A new look at the transition state: Wigner's dynamical perspective revisited. Adv Chem Phys 2005;130:171.
[34] Wiesenfeld L. Geometry of phase-space transition states: Many dimensions, angular momentum. Adv Chem Phys 2005;130:217.
[35] Wiggins S, Wiesenfeld L, Jaffé C, Uzer T. Impenetrable barriers in phase-space. Phys Rev Lett 2001;86:5478.
[36] Waalkens H, Burbanks A, Wiggins S. Phase space conduits for reaction in multidimensional systems: HCN isomerization in three dimensions. J Chem Phys 2004;121:6207.
[37] Aguirre J, Vallejo JC, Sanjuán MAF. Wada basins and chaotic invariant sets in the hénon-heiles system. Phys Rev E 2001;64:066208.
[38] Blesa F, Seoane J, Barrio R, Sanjuán MAF. To escape or not to escpace, that is the question. perturbing the hénon-heiles. Int J Bifurcation Chaos 2012;22:1230010.
[39] Martens EA, Panaggio MJ, Abrams DM. Basins of attraction for chimera states. New J Phys 2016;18:022002.
[40] Santos Vdos, Borges FS, Iarosz KC, Caldas IL, Szezech JD, Viana RL, et al. Basin of attraction for chimera states in a network of rössler oscillators. Chaos 2020;30:083115.
[41] Daza A, Georgeot B, Guéry-Odelin D, Wagemakers A, Sanjuán MAF. Chaotic dynamics and fractal structures in experiments with cold atoms. Phys Rev A 2017;95:013629.
[42] Ernst A, Peters T. Fractal basins of escape and the formation of spiral arms in a galactic potential with a bar. Mon Not R Astron Soc 2014;443:2579.
[43] Sweet D, Ott E, Yorke J. Topology in chaotic scattering. Nature 1999;399:315.
[44] Daza A, Wagemakers A, Sanjuán MAF, Yorke JA. Testing for basins of wada. Sci Rep 2015;5:16579.
[45] Daza A, Wagemakers A, Georgeot B, Guéry-Odelin D, Sanjuán MAF. Basin entropy: a new tool to analyze uncertainty in dynamical systems. Sci Rep 2016;6:31416.
[46] Kennedy J, Yorke JA. Basins of wada. Physica D 1991;51:213.
[47] Nusse HE, Yorke JA. Wada basin boundaries and basin cells. Physica D 1996;90:242.
[48] Nusse HE, Yorke JA. Fractal basin boundaries generated by basin cells and the geometry of mixing chaotic flows. Phys Rev Lett 2000;84:626.
[49] Hénon M, Heiles C. The applicability of the third integral of motion: Some numerical experiments. Astron J 1964;69:73.
[50] Gutzwiller MC. Chaos in classical and quantum mechanics. New York: Springer-Verlag; 1990.
[51] Danby JMA. Fundamentals of celestial mechanics. 2nd ed.. Richmond, Virginia: Willmann-Bell; 1992.
[52] Lanchares V, Pascual AI, Iñarrea M, Salas JP, Palacián JF, Yanguas P. Reeb's theorem and periodic orbits for a rotating hénon-heiles potential. J Dyn Diff Equat 2021;33:445.
[53] Iñarrea M, Lanchares V, Palacián JF, Pascual AI, Salas JP, Yanguas P. Lyapunov stability for a generalized hénon-heiles system in a rotating reference frame. Appl Math Comput 2015;253:159.
[54] Meyer KR, Hall GR. Introduction to Hamiltonian dynamical systems and the N-body problem. In: Applied mathematical sciences. New York: Springer-Verlag; 1992.